This is a repository copy of *Casting homogeneity of scaled-up multiprincipal component alloys*.

White Rose Research Online URL for this paper:
https://eprints.whiterose.ac.uk/223138/

Version: Published Version

Article:
Adeyemi, G.J., Utton, C., Azakli, Y. et al. (1 more author) (2025) Casting homogeneity of scaled-up multiprincipal component alloys. Journal of Manufacturing and Materials Processing, 9 (2). 41. ISSN 2504-4494

https://doi.org/10.3390/jmmp9020041

Reuse
This article is distributed under the terms of the Creative Commons Attribution (CC BY) licence. This licence allows you to distribute, remix, tweak, and build upon the work, even commercially, as long as you credit the authors for the original work. More information and the full terms of the licence here:
https://creativecommons.org/licenses/

Takedown
If you consider content in White Rose Research Online to be in breach of UK law, please notify us by emailing eprints@whiterose.ac.uk including the URL of the record and the reason for the withdrawal request.

eprints@whiterose.ac.uk
https://eprints.whiterose.ac.uk/

Journal of
Manufacturing and Materials Processing

MDPI

Article

Casting Homogeneity of Scaled-Up Multiprincipal Component Alloys

Gbenga. J. Adeyemi [1,*], Claire Utton [2], Yunus Azakli [2] and Russell Goodall [2]

[1] Department of Mechanical Engineering, Ekiti State University, Ado-Ekiti 362103, Nigeria
[2] School of Chemical, Materials and Biological Engineering, The University of Sheffield, Mappin Street, Sheffield S1 3JD, UK; c.utton@sheffield.ac.uk (C.U.); y.azakli@sheffield.ac.uk (Y.A.); r.goodall@sheffield.ac.uk (R.G.)
* Correspondence: gbenga.adeyemi@eksu.edu.ng

Abstract: High-entropy and multicomponent alloys are believed to offer opportunities for improved properties and are currently of great interest to the research community. Studies on these materials are largely conducted on small samples, but, for many practical applications, larger-scale processing would be needed. The processing of metallic parts of high dimensionality conventionally begins with casting, but an increase in the scale of the melt increases the potential for effects dependent on segregation, diffusion and thermal transport. The objective here is to determine the effect of scale-up on the as-cast condition of an example multicomponent alloy, Cu-Zn-Mn-Ni medium-entropy (ME) brass, in a larger quantity. The ingot was produced by metallic mould casting after induction melting. The hardness, microstructures and chemical composition were assessed in the as-cast state across a section through the material. A range of hardness values were found, particularly in the vertical direction, where the upper region was found to have a hardness of 188 ± 15 HV0.5, a middle of 161 ± 11 HV0.5 and a bottom of 184 ± 16 HV0.5. These values can be correlated with the casting conditions experienced locally, but the average hardness values are close to that of the original reports of the alloy. To overcome this, it is likely that a heat treatment would need to be used for this alloy in practical production before the products could be applied for engineering uses.

Keywords: multicomponent alloys; casting; hardness testing; microstructures; chemical composition

check for updates

Academic Editor: Steven Y. Liang

Received: 6 November 2024
Revised: 22 January 2025
Accepted: 28 January 2025
Published: 29 January 2025

Citation: Adeyemi, G.J.; Utton, C.; Azakli, Y.; Goodall, R. Casting Homogeneity of Scaled-Up Multiprincipal Component Alloys. *J. Manuf. Mater. Process.* **2025**, *9*, 41. https://doi.org/10.3390/jmmp9020041

Copyright: © 2025 by the authors. Licensee MDPI, Basel, Switzerland. This article is an open access article distributed under the terms and conditions of the Creative Commons Attribution (CC BY) license (https://creativecommons.org/licenses/by/4.0/).

1. Introduction

This work examines an equi-atomic Cu-Zn-Mn-Ni medium-entropy (ME) brass, previously reported in the literature. As the motivation for the investigation of such alloys comes from conventional brasses, these materials are briefly discussed, with the earlier reports of the specific alloy of interest then covered.

1.1. Traditional Brass Alloys

Brasses are copper–zinc alloys with a wide range of engineering uses. Additions of zinc to copper raise the strength and give a number of improvements to other properties, such that the brasses are a versatile range of materials. They are used for their strength, corrosion resistance, appearance and colour and ease of working and joining. The single-phase alpha brasses, containing up to about 37% zinc, are ductile and easy to hold work, weld and braze. The dual phase alpha-beta brasses are usually hot-worked [1].

Brasses are resistant to corrosion in many media, such as atmosphere and water, including salt water [2–4], though they can be susceptible to corrosion by solutions containing ammonia. Alloys with more than about 15% of zinc may suffer dezincification, which leaves a weak, porous corrosion deposit of copper. Resistance to dezincification is greatly reduced by the addition of a small amount of arsenic to the alloy. Stress corrosion cracking, particularly by ammonia and amines, is also a problem with the brasses. Alloys containing more than about 15% zinc are most susceptible. The use of a precipitation heat treatment and stress relieving after forming reduces the susceptibility to stress corrosion cracking [1]. As well as corrosion behaviour, brasses are characterised by a relatively low density, high electrical and thermal conductivities, and good formability, making brass important for various applications. Nevertheless, improvements to some of these properties, such as increased mechanical performance and wider spectrum corrosion resistance, are desirable, and this has motivated the exploration of high-entropy alloys based on brass-like compositions.

1.2. Multicomponent Brass Alloys

High entropy or multicomponent alloys [5–8] are those with multiple alloying elements, usually in similar atomic fractions [9,10], producing compositions that in some cases result in the formation of a single, highly alloyed phase. A number of potential advantages of HEAs over single-element-dominated alloys have been identified [11,12], such as high strength and hardness, good thermal stability, outstanding corrosion resistance, and high malleability and deformability [5,13].

Among these, the mechanical properties of the high-entropy metal alloys (which, due to their general similarity can also be looked for in multicomponent brass alloys) are sometimes found to be superior to traditional metal alloys. This is suggested to be due to the higher entropy of the solid solution increasing its microstructural stability, retaining a highly alloyed solid solution, which provides a high-strengthening effect, even in temperature increase. In practice, this microstructural stability depends on more than just the entropy, with the composition and solidification rate having a strong effect on the phases seen [14].

As a result, the casting techniques employed will play a significant role in the mechanical properties of the alloys. Casting is the process of pouring molten metal inside a mould cavity—in some cases, one created by a pattern—and allowing it to solidify to obtain the required size and shape component directly [15]. While the production of the shape is the desired part of the process, the conditions of the casting, including the type of mould, the temperature distribution, the atmosphere and many other factors will influence the result. This will include the grain structure and the defect population (comprising pores, oxide and other inclusions and segregation, among others), which also frequently vary with position in the casting in relation to how the interface between the liquid and solid proceeds through the volume. As larger-scale casts mean that the amount of thermal energy and the distances for heat and mass transport involved are larger, these problems tend to be exacerbated with size.

The research area of HEAs attracts much interest [16]. The specific term HEAs refers to alloys that are made up of five or more principal elements at various atomic percentages between 5 and 35% [17–19], and, where these apply to alloys containing Cu and typical brass elements like Zn, Ni and Mn, the materials may be referred to as high-entropy brasses. Where the strict HEA definition is not met, the term multiprincipal element brass may be more appropriate. Research work has been carried out on examples of multiprincipal component alloy brasses, and the effect that the modification of the composition has on the structure and properties [20,21]. Alloys that have been reported include CuMnZnNi [5], NiCoFeMnCrP [22] and many others.

As multicomponent alloys, including the multiprincipal component alloy brasses, develop towards applications, industrially applicable manufacturing processes will need to be adopted and used at scale. Most research work is none on small samples, of a few tens of grams in weight, but most applications will need, as a minimum, multikilogram melts to be economic. Casting is likely to be an important part of processing at these volumes, but the scale-up of cast processing can reveal different material behaviour and defects. There is little work reported in the literature on the scale-up of any multicomponent alloys, with, in some cases, scale-up being applied to the creation of as little as 250 g of an alloy [23]. Attempts that go to larger scale, such as the 25 kg cast of (CoCrFeMnNi)95Al5 reported in [24], do not examine different parts of the ingot to observe differences of structure, composition or defects. The present study has the goal of investigating what differences and defects are encountered, particularly looking at differences through the height of an ingot, on the scale-up of a multiprincipal component alloy.

To do this, the equiatomic Cu-Zn-Mn-Ni medium-entropy (ME) brass reported by Nagase et al. [5] was adopted. This alloy is a multiprincipal component alloy and could potentially find applications in many of the areas where brasses are applied. It also shows a two-phase microstructure according to published results, which increases the complexity of the microstructure that may form on casting over a single-phase solid solution but not to the extent of an alloy with multiple phases, which may be less desirable for applications. In our work, new samples of this alloy composition are made up from elemental material and cast in a conventional process, using a metal mould, producing an ingot of more than 4 kg. The initial report of this alloy was based on specimens cast in 20 mm diameter moulds, with approximately 30 mm height, so it is estimated, from the average density of the constituents, that this corresponds to around 300 g. The cast here represents a scale-up of more than an order of magnitude and allows the effects of length scale in casting and differences in cooling to be investigated experimentally in alloys of this type.

2. Prediction of Alloy Phase Structure

In order to guide the selection of the alloy and to provide a means to interpret the microstructures seen, the temperature-dependent phase stabilities of the selected alloy (equiatomic Cu-Zn-Mn-Ni) were examined with the use of Thermo-Calc 2 software, 2023b version, using the SSOL8 database. The obtained results from the software are presented in Figure 1.

As can be seen from Figure 1, the alloy shows a temperature range where it is predicted to have a single-phase FCC structure, between 662 °C and 991 °C. Below 662 °C, two-phase BCC and FCC are stable. Above 991 °C, melting begins, with the material being fully liquid above 1093 °C. The choice of this alloy was shown to be supported by thermodynamic considerations, with calculation clearly indicating the possibility of obtaining single-phase materials from the temperature-phase relationship shown in Figure 1, which would potentially result from the rapid cooling of the material once solid at temperatures above ~660 °C. Microstructural control could then be possible, using aging-type heat treatments at temperatures below this to nucleate and grow the BCC phase in a controlled manner, which might result in strengthening due to the introduction of phase boundaries.

These predictions could be consistent with published results on equiatomic CuZn-MnNi, which has shown single-phase structures [5], if it is considered plausible that, in the relatively rapid cooling rates that would be experienced in the smaller castings made previously, there would be insufficient time for the formation of the secondary phases at a low temperature.

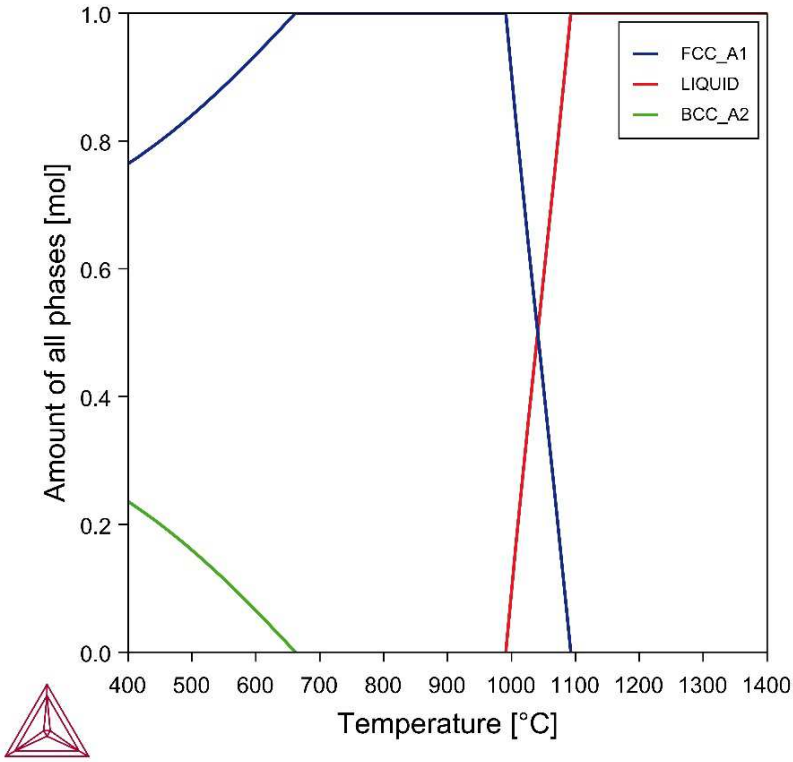

Figure 1. The predicted variation in phase fraction at equilibrium with temperature for equiatomic CuZnMnNi.

3. Materials and Methods

3.1. Ingot Processing

In this work, a single ingot of approximate dimensions 75 × 80 × 100 mm and mass of around 4 kg was created. While this does not allow the assessment of cast-to-cast variation, the amount of material represents a large increase over what has been previously made for this alloy and provides ample material for the investigation of different positions in the casting itself. It is also a size of casting/section thickness that could be the representative of some smaller components. The general experience is that casting is a reproducible process, and it is likely that other ingots produced with the same method would be consistent; though it should be noted that deviations from the process, such as different mould types, cast shape or volume, would give different solidification conditions and thus could cause different behaviour.

The alloy components of Cu, Ni, Mn and Zn, with a purity of 99.9% or higher and supplied by William Rowland Ltd., UK, were selected to ensure minimal deviations from the desired composition. The atomic and weight fractions of these elements are provided in Table 1. The elements were weighed using an electronic mass balance with an accuracy of two decimal places to produce slightly over 4 kg of the final alloy, ensuring precise measurements for the target composition. To compensate for evaporation losses, an additional 5% Zn was included in the batch.

Table 1. The ratios of elements employed for ingot fabrication.

Element	Atomic %	Atomic Weight	Weight %
Cu	25	63.54	26.19
Ni	25	58.69	24.19
Mn	25	54.93	22.64
Zn	25	65.39	26.95

The Cu, Ni and Mn components were placed in an alumina (Al_2O_3) crucible and melted in a vacuum induction melting system under an argon atmosphere. The vacuum chamber was evacuated to a pressure of 3×10^{-3} mbar, and the crucible was conditioned at low power under vacuum conditions. Before melting, the chamber was backfilled with argon to a pressure of 90 mbar. Once the charge was fully melted, the chamber was further backfilled with argon to a pressure of 600 mbar. The Zn was introduced into the melt 10 min prior to casting to minimise excessive evaporation losses.

At approximately 1200 °C, the molten alloy was cast into a BN-lined steel mould with a graphite base. The ingot was cooled to room temperature within the mould under an argon atmosphere to produce the ingot shown in the as-cast condition in Figure 2, with approximate dimensions of 75 × 80 × 100 mm.

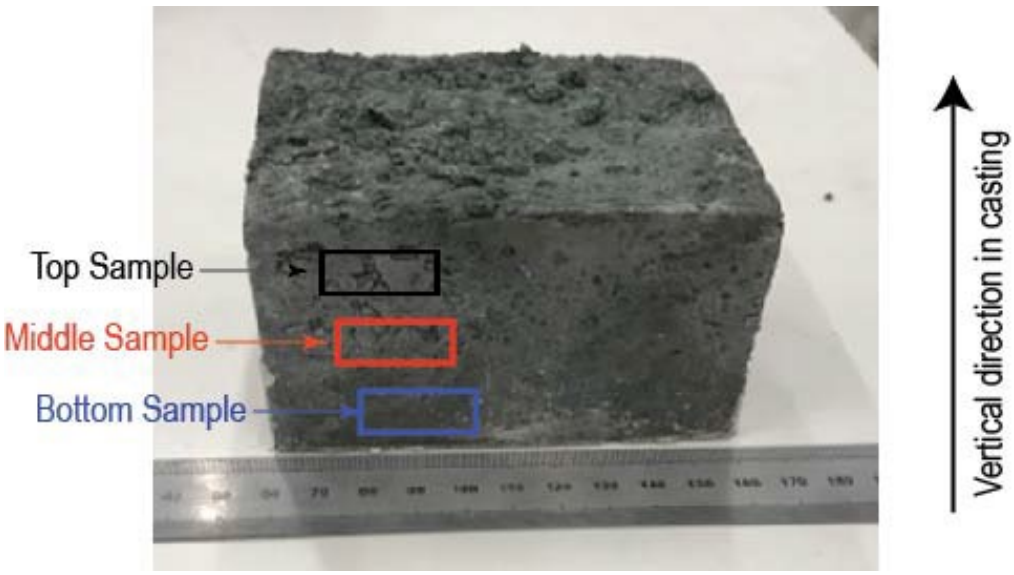

Figure 2. The as-cast ingot produced, showing the vertical direction during the casting process, and the approximate location of the different samples extracted.

The ingot produced was allowed to cool to room temperature in air before being sectioned vertically for the investigation.

3.2. Ingot Characterisation

From the as-cast ingot shown in Figure 2, a series of smaller sections were made, producing blocks of 10 mm × 15 mm × 20 mm, using a manual abrasive 250 cutter.

These sections were taken from different vertical positions in the original cast: the upper, middle and bottom regions. The metal block sample shown above was mounted into pellet of 30 mm diameter and 20 mm thickness, using Simplimet 1000 automatic mounting press machine, Beuhler, Leinfelden-Echterdingen, Germany.

Each of the samples obtained from the above section was ground in three steps using an Ecomet 250 Pro Grinder-Polisher, Beuhler, Leinfelden-Echterdingen, Germany. The first step used 22 N applied force, 5 g head and 300 base speeds, with P400 grit paper for 60 s. The second grinding stage used 21 N force with the same head and base speed and P1200 grit paper for 60 s. The final stage also used the same head and base speeds, with 20 N grinding force and P2500 grit paper for 60 s. The machine was in the compound direction, where the wheel rotates in the same direction as the samples during grinding.

Samples were then polished to metallographic quality with 3 µm diamond suspension using the contra machine direction, 10 N applied force, 45 and 150 head and base speeds for 300 s. A second stage of polishing used one 3 µm diamond suspension and contra machine

direction with 8 N applied force and the same head and base speeds. A final polishing stage used colloidal silicon dioxide with a grain size 0.06 μm and dropwise addition of water, with 8 N applied force for 300 s and 5 N applied force for 180 s.

The specimens were thoroughly rinsed with water and alcohol and dried after each grinding and polishing step to prevent possible carry-over of abraded particles and contaminations. After the final polishing, the sample was additionally cleaned in an ultrasonic bath for two minutes and then rinsed under running water and with alcohol and dried. The specimens were finally chemically etched before carried to the next line of action.

The hardness of the samples was investigated using a Durascan 70 machine, Struers, Champigny sur Marne cedex, France, with the application of 0.5 HV hardness force for each tested sample. Scanning Electron Microscopy (SEM), FEI Company, Hillsboro, OR, USA, was used for microstructures, X-ray Fluorescence (XRF) and Energy-Dispersive X-ray Spectroscopy (EDS) for composition determination, as described below.

3.2.1. Hardness

Vickers hardness evaluation was performed in line mode with 0.5 kg load (resulting in values of HV0.5), covering eighteen points distributed across the surface of the sample.

These were carried out to make sure that the hardness values across the surface of each of the zones were captured and evaluated. The process was repeated for the sample obtained from the middle and bottom of the ingot layers, respectively.

3.2.2. Scanning Electron Microscopy (SEM), X-Ray Diffraction XRD and X-Ray Fluorescence (XRF) Processing

Following the preparation of the samples previously described, samples were examined with the aid of an Inspect F50 Scanning Electron Microscope, FEI Company, Hillsboro, OR, USA. Both the microstructures and chemical properties of the sample were captured with the aid of an Oxford Instruments XMAX 80 detector (Abingdon, UK). The obtained image data were processed with Aztec software, Oxford Instruments, version 6.1, and presented for further analysis. Also, the chemical quantities of the entire surface of each layer were examined using X-ray Fluorescence (XRF). The elements obtained are presented for further analysis in the section below. The phases of those layers using the XRD machine were also examined and presented for further justification.

4. Results and Discussion

The data obtained from both hardness machine and Energy-Dispersive X-ray Spectroscopy were analysed and presented in this section.

4.1. Results

4.1.1. Hardness Evaluation

The hardness values obtained across the tested samples are presented in Figure 3 below. Hardness measurements typically show variability so the results from each of the sectioned layers were first explored to check for any systematic variations within the matrix of indents used (for example, differences between the values in a different row or columns). As none were identified, all 17 values were averaged to produce the following data for the hardness of each section (with standard deviation given in brackets): upper, HV 188 ± 15; middle, HV 161 ± 11; bottom, HV 184 ± 16.

The hardness values showed a similar variability in each position, with the values and range for the top and bottom of the casting being very consistent. While the distribution of the values recorded in the centre does overlap with these positions, it appears that, on the whole, the hardness is lower in this region. This can be further tested by treating the data statistically and looking at the results of a *t*-Test. Performing the test gives a *t*-value

of $t(16) = 5.984$, $p < 0.00001$ when comparing middle and top datasets of hardness results and a t-value of $t(16) = 5.046$, $p < 0.00001$ for the comparison between middle and bottom datasets. In each case, this indicates a significant difference between the two datasets considered in each pair. On the other hand, the t-value comparing the top and bottom datasets is only $t(16) = 0.746$, $p = 0.23045$, indicating the two groups are in this case similar.

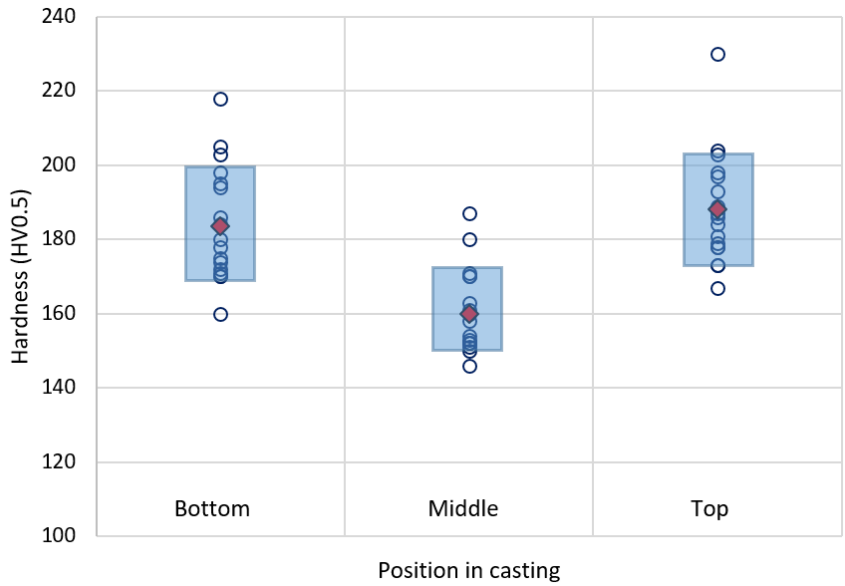

Figure 3. Hardness values of different regions in the vertical direction of as-cast equiatomic Cu-Zn-Mn-Ni. Each tested point is shown as an open circle, with the mean indicated as a red triangle and the box indicating the range of ±1 standard deviation.

4.1.2. Microstructure

Scanning Electron Microscopy was used to examine the microstructure at each point. Figure 4A–C shows typical microstructures from the top, middle and bottom layers, respectively.

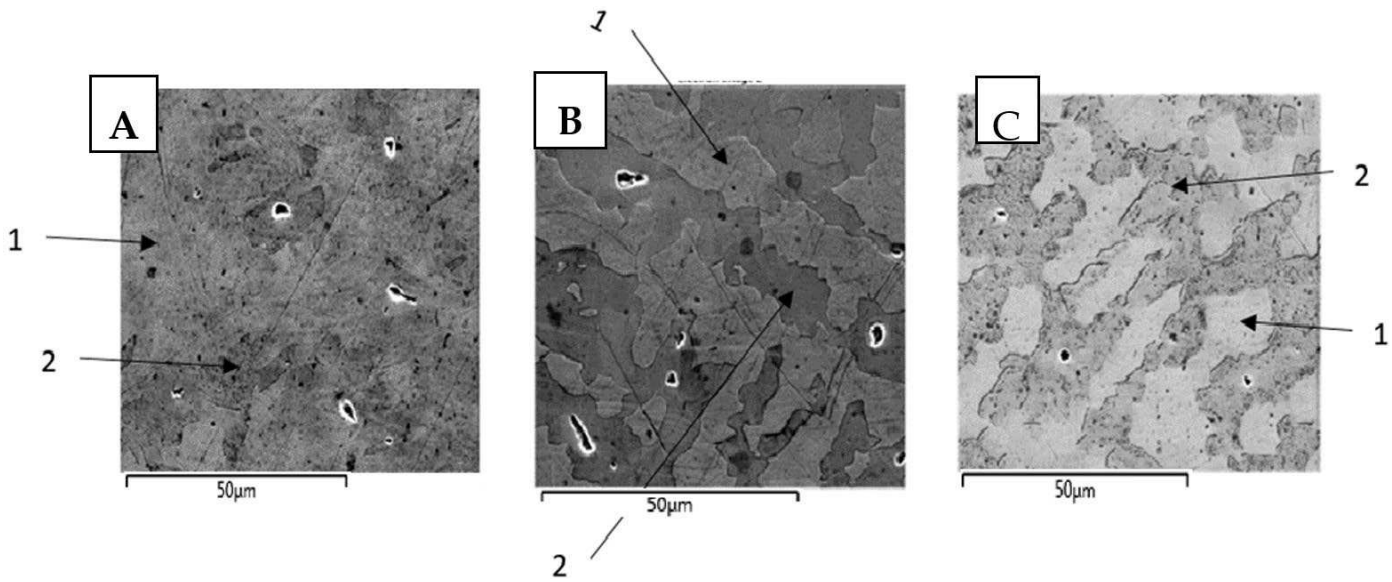

Figure 4. Typical microstructures obtained by SEM from the as cast equiatomic Cu-Zn-Mn-Ni: (**A**), the top region, (**B**) the centre region and (**C**) the bottom region.

The microstructures in Figure 4 show a lighter contrast phase with a dendritic structure (indicated by 1) and darker contrast inter-dendritic regions (indicated by 2). For the

microstructure of the top layer (Figure 4A), most of the material is the lighter dendritic phase with only a small proportion being the inter-dendritic phase. Apart from an apparent difference in the proportion of phases, the same type and scale of microstructure are shown in both the middle and bottom layers.

Although a sufficiently large set of images for detailed quantification has not been obtained at this stage, it is possible to make an initial assessment of the grain size of the material under the middle layer (which seems comparable to the other positions). Performing the linear intercept method on these images gives an average size for phase 1 regions of 29.8 μm (with 95% confidence limits of ±4.4 μm) and phase 2 regions of 24.4 μm (with 95% confidence limits of ±3.6 μm).

It should be noted that microstructures of the general form observed throughout the casting here are likely to be positive for strength, containing a large density of interfaces that can be a barrier to dislocation motion, due to the dendritic form and also due to the finer-scale structure that seems to be present in the interdendritic phase.

4.1.3. X-Ray Diffraction of the Layers

The X-ray reflection obtained from the different layers of the ingot mentioned above is shown in Figure 5.

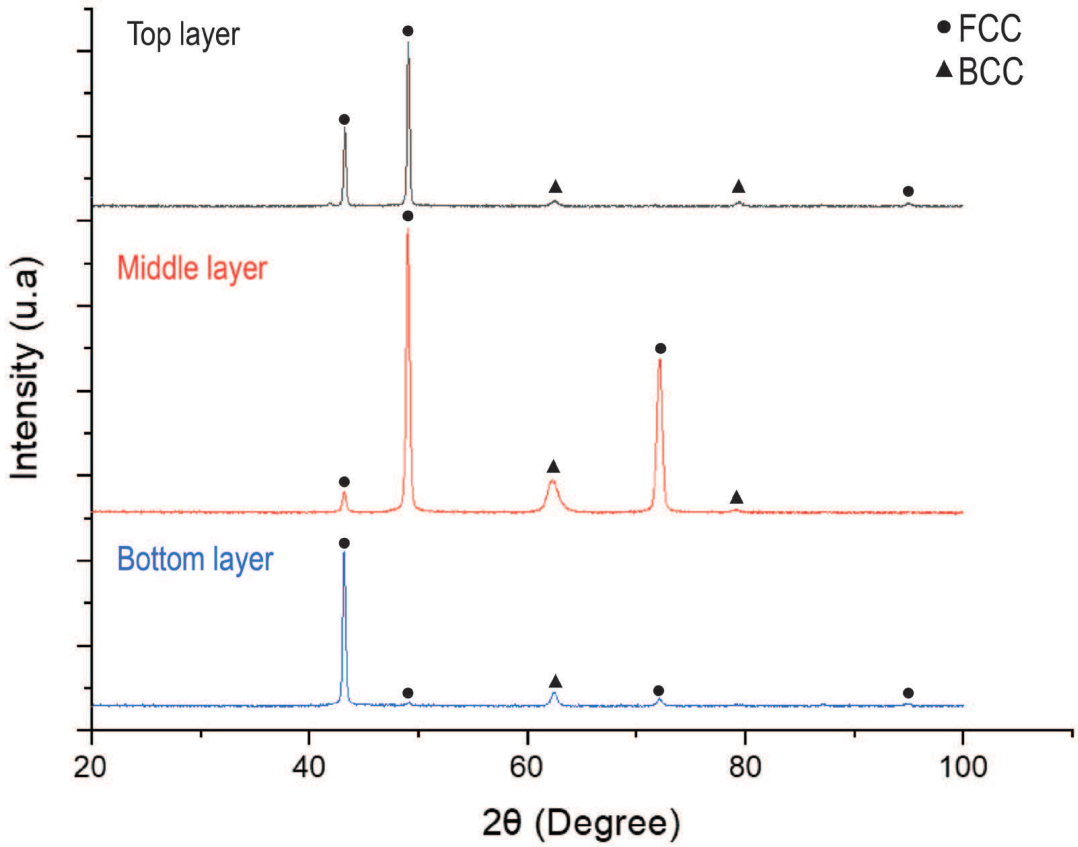

Figure 5. The XRD diffraction patterns obtained from the as-cast equiatomic Cu-Zn-Mn-Ni.

The black graph in Figure 5 shows the pattern from the top layer of the ingot. This shows multiple reflections, which are consistent with those in the pattern from the bottom layer (blue graph). Therefore, the graphs shown above indicate that both layers are of the same dual phases (FCC and BCC); the intensity varies due to the fact that these are as cast samples; therefore, there is not the ideal mixture of large numbers of different crystal orientations as there would be in a powder XRD sample.

4.1.4. Composition

The chemical composition of the material was obtained from each of the vertical positions with the aid of Energy-Dispersive X-ray Spectroscopy for each phase present to examine differences in partitioning. Also, X-ray Fluorescence was used to obtained chemical composition from the entire surfaces of each layer to capture overall chemical variation and explore macrosegregation. The results obtained from both processes are presented below. The chemical compositions of each of the two phases observed from the different vertical positions are summarised in Table 2. In interpreting these results, several aspects of the EDX technique need to be kept in mind. Although results are presented as their average values to 1 dp, the actual equipment accuracy is limited to around ±1 at%. In addition, the small number of points recorded means that standard deviations are not considered reflective of actual data and are not presented. These factors, which could act to accentuate differences, can be set against possible inaccuracy from the scale of the microstructure. This is relatively fine, with dendrite arms that are on the order of 10 microns, and so, considering the interaction volume from which the EDX signal is produced is likely to be around 1 micron across, there is a significant possibility that any point scan will include data from more than one phase region; this effect would tend to diminish compositional differences between phases.

Table 2. The EDX compositional results for different phases of the vertical layers of the alloys. Values are quoted to 1 dp, but the equipment accuracy is taken as ±1 at%.

Layers	Element Content (Atomic %)				
	Phase	Ni	Cu	Zn	Mn
TOP	1	26.5	25.1	24.4	24.0
	2	21.5	27.6	28.5	22.3
MIDDLE	1	28.7	24.8	23.8	22.7
	2	29.1	28.7	21.7	20.4
BOTTOM	1	26.9	24.9	24.2	24.0
	2	20.6	29.6	28.1	20.6

Taking these limitations into account, these results indicate that Ni and Mn may have a tendency to be enriched in the dendrite region (1) while the inter-dendritic region (2) may be enriched in Cu and Zn; this tendency is largely consistent across the height of the sample. There is also an apparent variation in the partitioning of the elements Ni, Zn and Mn in the middle of the casting compared to the top and bottom, but, considering the possible limitations on the accuracy discussed above, this point can be checked by an alternative technique, XRF, which obtains a signal over a much larger area of specimen and is, therefore, much less affected by point-to-point variations in composition. These data are presented in Table 3.

Table 3. The XRF compositional results for different vertical positions in the ingot.

Layers	Element Content (Atomic %)			
	Ni	Cu	Zn	Mn
TOP	25.12	26.36	24.12	23.44
MIDDLE	25.10	26.37	24.22	23.42
BOTTOM	25.19	26.34	24.13	23.42

These results show that the overall composition was very consistent across the casting, with very little variation in composition in any of the elements. While it is still possible that

microsegregation differences between the different samples is the origin of the hardness differences observed, this evidence indicates that macrosegregation, at least between the centre and the upper and lower regions, is not present in this sample.

4.2. Discussion

The highest average hardness values (188 HV and 184 HV) were found in the top and bottom layer, with a lower average hardness in the middle of the casting (161 HV), and, as reported in the analysis, the data collected in the middle region are significantly different to that from the top and bottom. The origin of this difference is likely to result from the lower cooling rate experienced in the centre of the casting as the lower part will experience more rapid cooling through the mould and the upper by heat loss to the casting chamber. More rapid cooling can affect alloys to increase hardness, but this can affect the material in a number of different ways, and, in some systems, where the effect is large, it will depend on the availability of non-equilibrium transformations [3,25].

In the current case, the predicted phase diagram (Figure 1) does not indicate that such a transformation would be possible. Changes in microstructural scale can also occur with the cooling rate, with more rapid cooling limiting transport by diffusion, and this leading to refined microstructures, which, where they limit dislocation mobility, would increase the strength, but the micrographs here show structures of similar sizes in each zone. It is, therefore, possible that minor variations, or more likely features of the structure on a finer scale than that resolvable in the SEM, are the cause. Fine precipitates, which require Transmission Electron Microscopy (TEM) to be observed give significant contributions to strength in many metallurgical systems of practical interest, including steels and some aluminium alloys, for example.

Another factor leading to the different hardness in the middle of the ingot that depends on the heat flow, but results from other processes, is the process of solidification itself. The initial material to freeze will be around the outside of the mould and at the surface where heat is lost most rapidly, and the last material to solidify is likely to be located towards the centre. This phenomenon is common in castings and can lead to macrosegregation and the concentration of some elements and defects either towards or away from the centre. The absence of any observed compositional difference from XRF suggests that this is not the case (though there could still be a non-uniform distribution of porosity or inclusions), but where dendritic growth occurs, as observed in the micrographs here, there is also the possibility of segregation on a microscale. In this context, the occurrence of different degrees of the separation of elements into the different phases in the ingot between the edges and the centre, which appears to be the case from the local EDX measurements of the composition of each phase, is suggestive that microsegregation may be happening, and the degree may be affected by the cooling rate. If the composition of the two phases is altered by this microsegregation, then this could give rise to changes in the ease of plastic deformation (for example, by changing the degree of solid solution strengthening, changing the stacking fault energy and thus influencing the formation of partial dislocations or through inhomogeneous distributions contributing to a variable landscape that is harder for dislocations to traverse) and be responsible for the hardness differences seen.

To explore the consequences of these variations further, additional predictions were made using Thermo-Calc software v.2024a and the SSOL8: SGTE Alloy solutions database v.8. Both equilibrium and non-equilibrium calculations (Scheil simulation) were performed. Equilibrium calculations were performed for the actual compositions of phases 1 and 2 with aid of the chemical composition obtained from the top, middle and bottom layers of the ingot, as shown in Table 3 above. The results are shown in Figure 6 below. If the predictions were correct and the sample was fully at equilibrium, each composition should predict a

single phase to be formed, corresponding to the phase that was identified, but, in most cases, this is not the outcome, indicating either inaccuracy in the prediction or non-equilibrium compositions. The predictions for phase 1 (the top line in the figure) are all consistent, suggesting that there is no significant change to be expected from the compositional differences occurring here. Phase 2 on the other hand shows similar predictions (for two-phase structures of FCC and BCC A2) when the top and bottom compositions are used but a single-phase prediction (FCC) from the middle composition. This may suggest that the composition of phase 2 in the middle is closer to equilibrium, as would be expected if the slower cooling rate produced less microsegregation.

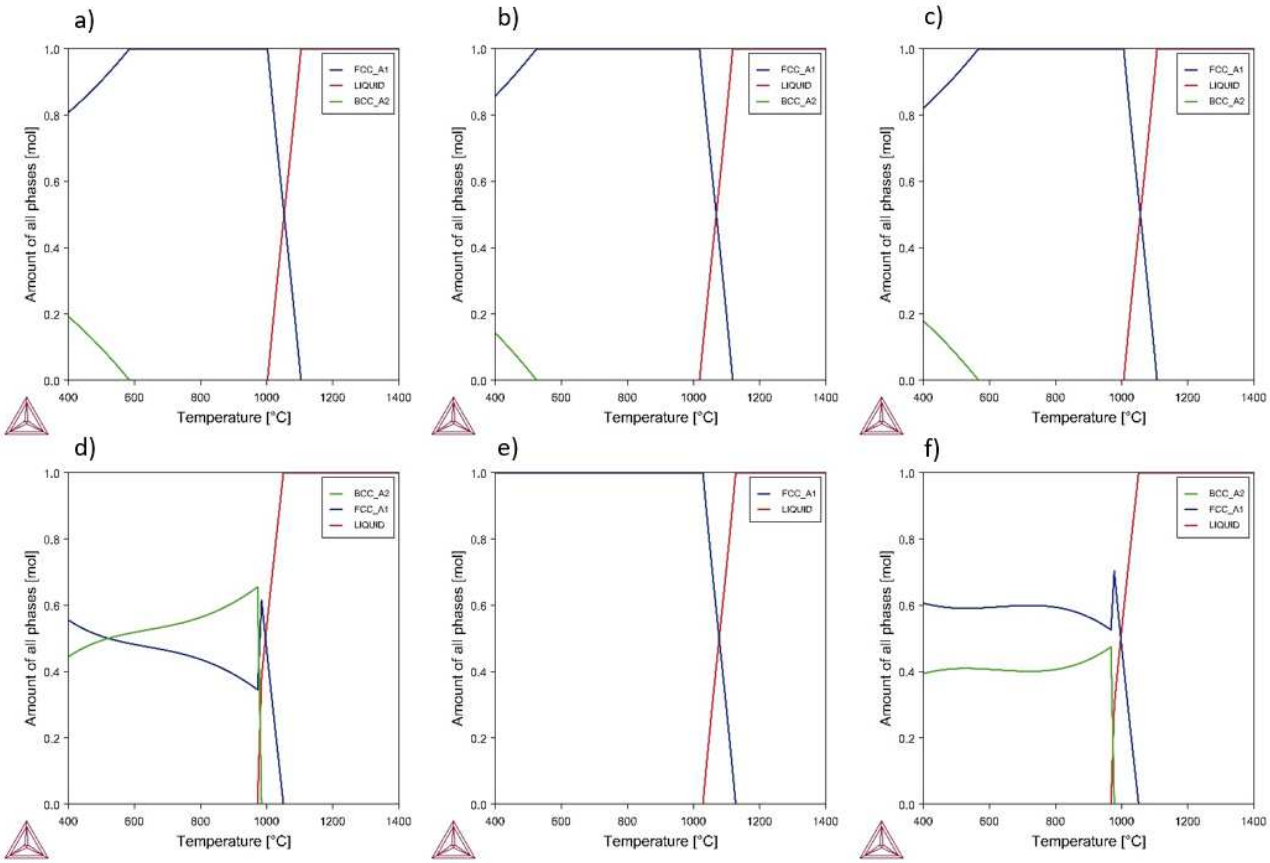

Figure 6. The Thermo-Calc predictions of the equilibrium phases with temperature for the actual measured compositions for phase 1 (top row) and phase 2 (bottom row) in the ingot; (**a**,**d**) top surface, (**b**,**e**) middle and (**c**,**f**) bottom surface.

The results of modelling the measured composition of each region are shown in Figure 7. These show no observable variations between the regions and match well the calculation from Figure 1 of the nominal composition, which is rational considering the limited compositional change detected between the regions and the limited difference from the nominal composition. These all suggest the formation of a two-phase microstructure at equilibrium, which is consistent with the microstructural observations made of the material.

In addition, a non-equilibrium Scheil simulation was also performed for the nominal composition of the alloy (Figure 8). The simulation predicts that the FCC primary phase will form initially at 1093 °C, followed by the BCC phase at 974 °C. This shows that under more realistic, nonequilibrium conditions, as will be experienced in practice (and to differing degrees in a large casting), the system will retain liquid to lower temperatures than expected in the case of this prediction not becoming fully solid until around 880 °C. This occurs due to incomplete mixing in the solid, meaning that the remaining liquid becomes enriched beyond the equilibrium value in elements that are relatively less stable in the solid phase.

From the prediction, this segregation can also induce the BCC phase to form at higher temperatures and thus earlier in solidification than expected. It also demonstrates that as this effect occurs, differences in the degree of segregation with cooling conditions, as observed here, could occur. The Scheil simulation predicts the partitioning of Ni initially to the FCC phase and Cu and Zn to the BCC phase, which agrees qualitatively with the EDS and XRF analysis (Tables 2 and 3) of the two phases formed at the top and bottom of the ingot where cooling is expected to be fastest.

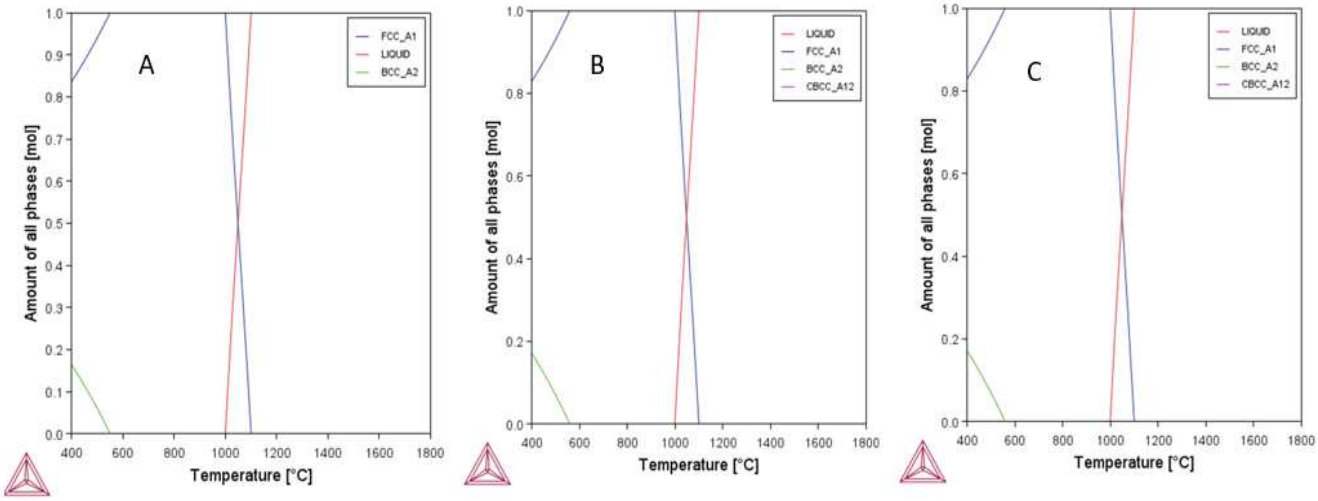

Figure 7. The Thermo-Calc predictions of the equilibrium phases with temperature for the actual measured compositions of the full region; (**A**) top layer, (**B**) middle layer and (**C**) bottom layer.

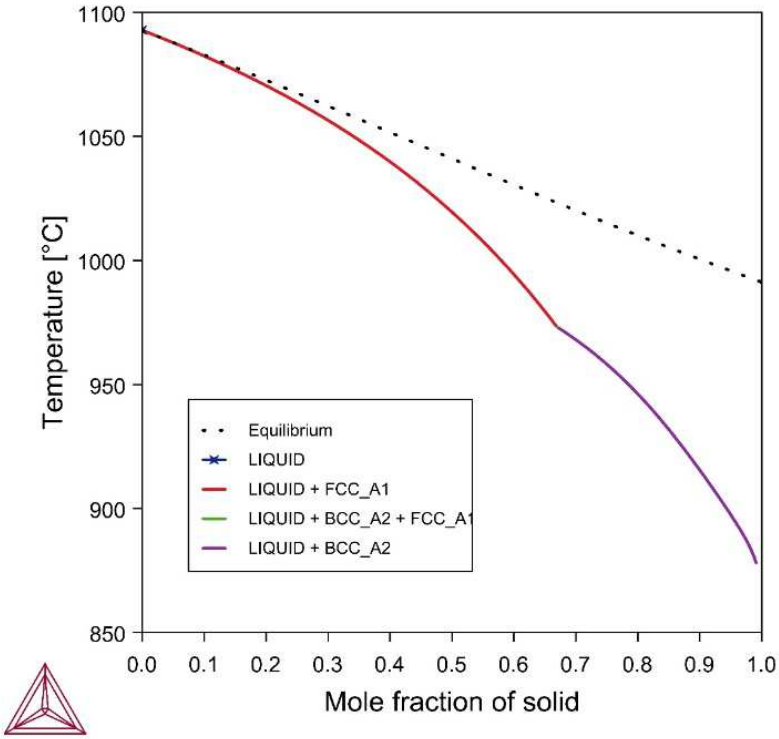

Figure 8. Scheil simulation for equiatomic Cu-Zn-Mn-Ni alloy.

The variations in hardness values seen were not initially expected. Although the differences in the average values obtained from each layer were not large, there is still a trend for reduced values in the middle. While microstructural differences due to the

thermal history must be considered, it is also possible that compositional differences could form. These could be as follows:

- Vaporisation losses of volatile elements despite the addition of an excess of these; if these losses differed from the expected amount, the overall composition of the alloy, and thus the properties, would be affected. For example, zinc was added in excess due to its high evaporation rate and is present in some regions above and in some below the required amount. In some alloy systems, increased zinc content can increase tensile strength and hardness but decrease ductility [26]. However, the XRF results confirm that this was not the case in the present alloy.
- The segregation of the elements on solidification, with the rejection of some elements in advance of the solidifying interface, leading to them being concentrated in the liquid. While no macrosegregation is detected in the XRF results, the differences in the compositions of the different phases in different places suggests that some microsegregation may be occurring and that the degree of this may differ from the edges to the centre. This may also contribute to the differences in hardness observed.

It should also be noted that the highest average hardness value found in this research (188.2 HV) is below that recorded by Nagase et al. [5] for nominally the same alloy (229 HV). The principal difference here is the quantity of material processed (we estimate that the quantity used in this work is more than an order of magnitude greater than in the earlier report). We have noted lower hardness occurring in the middle region of the ingot, which corresponds to conditions that would not have been achieved in the earlier sample. It is thus logical that, overall, a lower hardness would have resulted in the present case. These variations are likely to be resolvable with heat treatment as they are relatively minor.

5. Conclusions

In scale-up of materials, properties achieved in the laboratory do not always directly translate to production. To assess this in the case of multiprincipal component alloys, this work has produced an as-cast ingot of equiatomic Cu-Zn-Mn-Ni at a scale of >4 kg, an order of magnitude larger that has previously been produced for this alloy. This finds that the ingot is generally homogenous in phase structure and microstructure and does not display macrosegregation. The hardness shows variation in the vertical direction, with the centre position having hardness measures which are, on average, about 13% below the top and bottom regions. This was not seen in the original study of this alloy and may originate from the different microsegregations caused by differences in the conditions between the centre and edges of the casting.

Such a variation would not, in most cases, be desirable, producing uncertainty in the product, and would suggest that homogenisation heat treatments would be required should these variations persist after any further mechanical deformation methods that were applied. As such, variations were not reported when the alloy was initially specified. It also indicates that the degree of such variation is dependent on the size of casting and/or the casting procedure used, and this must be borne in mind in work to scale-up multicomponent and high-entropy alloys for applications. Further examination of such materials after deformation and heat treatments, as are commonly applied to alloys produced in larger castings, is required in order to assess the impact of these variations from the casting stage on downstream processes.

Author Contributions: G.J.A.: Methodology, Investigation, Writing—Original Draft and Funding Acquisition; C.U.: Formal Analysis and Writing—Review and Editing; Y.A.: Investigation and Writing—Review and Editing; R.G.: Conceptualisation, Formal Analysis and Writing—Review and Editing. All authors have read and agreed to the published version of the manuscript.

Funding: G.J.A. would like to acknowledge funding from the University of Sheffield's International Visitor Support Scheme. Casting work within this article was supported by the Engineering and Physical Sciences Research Council (grant number EP/P02470X/1, EP/P025285/1, EP/R00661X/1, EP/S019367/1, EP/W006839/1 and EP/X527257/1).

Data Availability Statement: The data that support the findings of this study are available from the corresponding author, G.J.A., upon reasonable request.

Conflicts of Interest: All authors declare that they have no conflicts of interest.

References

1. Khanna, O.P. *A Textbook of Foundry Technology, Revised Edition*; Dhaupat Rai Ltd.: New Delhi, India, 1997.
2. William, D.C. *Material Science and Engineering: An Introduction*, 4th ed.; John Willey and Sons, Inc.: New York, NY, USA, 1997.
3. Rajan, T.V.; Sharma, C.P.; Sharma, A. *Heat Treatment Principles And Techniques*; Prentice Hall of India Private Limited: New Delhi, India, 1988.
4. Kroes, M.J.; Rardon, J.R. *Aircraft Basic Science*, 7th ed.; Glencoe/McGraw-Hill: New York, NY, USA, 1993.
5. Nagase, T.; Shibata, A.; Matsumuro, M.; Takemura, M.; Semboshi, S. Alloy design and fabrication of ingots in Cu-Zn-Mn-Ni-Sn high-entropy and Cu-Zn-Mn-Ni medium-entropy brasses. *Mater. Des.* **2019**, *181*, 107900. [CrossRef]
6. Cui, P.; Ma, Y.; Zhang, L.; Zhang, M.; Fan, J.; Dong, W.; Yu, P.; Li, G.; Liu, R. Effect of Ti on microstructures and mechanical properties of high entropy alloys based on CoFeMnNi system. *Mater. Sci. Eng. A* **2018**, *737*, 198–204. [CrossRef]
7. Cantor, B.; Chang, I.T.H.; Knight, P.; Vincent, A.J.B. Microstructural development in equiatomic multicomponent alloys. *Mater. Sci. Eng. A* **2004**, *375*, 213–218. [CrossRef]
8. Yeh, J.W.; Chen, S.K.; Lin, S.J.; Gan, J.Y.; Chin, T.S.; Shun, T.T.; Tsau, C.H.; Chang, S.Y. Nanostructured high-entropy alloys with multiple principal elements: Novel alloy design concepts and outcomes. *Adv. Eng. Mater.* **2004**, *6*, 299–303. [CrossRef]
9. Miracle, D.B.; Senkov, O.N. A critical review of high entropy alloys and related concepts. *Acta Mater.* **2017**, *122*, 448–511. [CrossRef]
10. Daoud, H.M.; Manzoni, A.M.; Wanderka, N.; Glatzel, U. High-temperature tensile strength of $Al_{10}Co_{25}Cr_8Fe_{15}Ni_{36}Ti_6$ compositionally complex alloy (high-entropy alloy). *JOM* **2015**, *67*, 2271–2277. [CrossRef]
11. Pavithra, C.L.; Dey, S.R. Advances on multi-dimensional high-entropy alloy nanoarchitectures: Unconventional strategies and prospects. *Nano Sel.* **2023**, *4*, 48–78. [CrossRef]
12. Gwalani, B.; Gangireddy, S.; Shukla, S.; Yannetta, C.J.; Valentin, S.G.; Mishra, R.S.; Banerjee, R. Compositionally graded high entropy alloy with a strong front and ductile back. *Mater. Today Commun.* **2019**, *20*, 100602. [CrossRef]
13. Dąbrowa, J.; Danielewski, M. State-of-the-art diffusion studies in the high entropy alloys. *Metals* **2020**, *10*, 347. [CrossRef]
14. Sonar, T.; Ivanov, M.; Trofimov, E.; Tingaev, A.; Suleymanova, I. An overview of microstructure, mechanical properties and processing of high entropy alloys and its future perspectives in aeroengine applications. *Mater. Sci. Energy Technol.* **2024**, *7*, 35–60. [CrossRef]
15. Shivkumar, S.; Wang, L.; Apelian, D. Molten metal processing of advanced cast aluminum alloys. *JOM* **1991**, *43*, 26–32. [CrossRef]
16. He, Q.F.; Ding, Z.Y.; Ye, Y.F.; Yang, Y.C. Design of high-entropy alloy: A perspective from nonideal mixing. *JOM* **2017**, *69*, 2092–2098. [CrossRef]
17. Tsai, M.-H.; Yeh, J.-W. High-entropy alloys: A critical review. *Mater. Res. Lett.* **2014**, *2*, 107–123. [CrossRef]
18. Zhang, Y.; Zuo, T.T.; Tang, Z.; Gao, M.C.; Dahmen, K.A.; Liaw, P.K.; Lu, Z.P. Microstructures and properties of high-entropy alloys. *Prog. Mater. Sci.* **2014**, *61*, 1–93. [CrossRef]
19. Otto, F.; Yang, Y.; Bei, H.; George, E.P. Relative effects of enthalpy and entropy on the phase stability of equiatomic high-entropy alloys. *Acta Mater.* **2013**, *61*, 2628–2638. [CrossRef]
20. Balaji, V.; Xavior, A. Development of high entropy alloys (HEAs): Current trends. *Heliyon* **2024**, *10*, e26464.
21. Pandey, V.; Seetharam, R.; Chelladurai, H. A comprehensive review: Discussed the effect of high-entropy alloys as reinforcement on metal matrix composite properties, fabrication techniques, and applications. *J. Alloys Compd.* **2024**, *1002*, 175095. [CrossRef]
22. Lai, D.; Kang, Q.; Gao, F.; Lu, Q. High-entropy effect of a metal phosphide on enhanced overall water splitting performance. *J. Mater. Chem. A* **2021**, *9*, 17913–17922. [CrossRef]
23. Puglielli, F.; Mussi, V.; Cugini, F.; Sarzi Amadè, N.; Solzi, M.; Bennati, C.; Fabbrici, S.; Albertini, F. Scale-Up of Magnetocaloric NiCoMnIn Heuslers by Powder Metallurgy for Room Temperature Magnetic Refrigeration. *Front. Energy Res.* **2020**, *7*, 150. [CrossRef]
24. Kumar, J.; Nayan, N.; Gupta, R.K.; Munisamy, M.R.; Biswas, K. High Entropy Alloys: Laboratory to Industrial Attempt. *Int. J. Met.* **2023**, *17*, 860–873. [CrossRef]

25. Shaikh, A.; Kumar, S.; Dawari, A.; Kirwai, S.; Patil, A.; Singh, R. Effect of temperature and cooling rates on the α + β morphology of Ti-6Al-4V alloy. *Procedia Struct. Integr.* **2019**, *14*, 782–789. [CrossRef]
26. Li, G.; Yang, H.; Zheng, Y.; Chen, X.H.; Yang, J.A.; Zhu, D.; Ruan, L.; Takashima, K. Challenges in the use of zinc and its alloys as biodegradable metals: Perspective from biomechanical compatibility. *Acta Biomater.* **2019**, *97*, 23–45. [CrossRef]

Disclaimer/Publisher's Note: The statements, opinions and data contained in all publications are solely those of the individual author(s) and contributor(s) and not of MDPI and/or the editor(s). MDPI and/or the editor(s) disclaim responsibility for any injury to people or property resulting from any ideas, methods, instructions or products referred to in the content.